



Universiteit
Leiden
The Netherlands

Effect of sphingosine and phytosphingosine ceramide ratio on lipid arrangement and barrier function in skin lipid models.

Nadaban, A.; Rousel, J.; El Yachioui, D.; Gooris, G.S.; Beddoes, C.M.; Dalgliesh, R.M.; ... ; Bouwstra, J.A.

Citation

Nadaban, A., Rousel, J., El Yachioui, D., Gooris, G. S., Beddoes, C. M., Dalgliesh, R. M., ... Bouwstra, J. A. (2023). Effect of sphingosine and phytosphingosine ceramide ratio on lipid arrangement and barrier function in skin lipid models. *Journal Of Lipid Research*, 64(8). doi:10.1016/j.jlr.2023.100400

Version: Publisher's Version

License: [Creative Commons CC BY-NC-ND 4.0 license](https://creativecommons.org/licenses/by-nc-nd/4.0/)

Downloaded from: <https://hdl.handle.net/1887/3640503>

Note: To cite this publication please use the final published version (if applicable).

Effect of sphingosine and phytosphingosine ceramide ratio on lipid arrangement and barrier function in skin lipid models

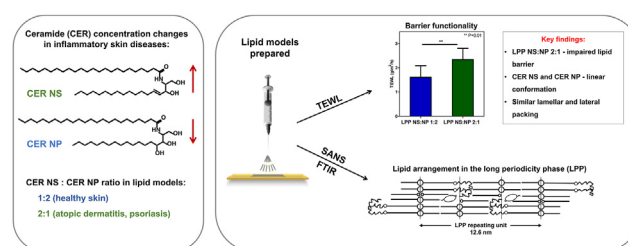
Andreea Nădăban¹, Jannik Rousel^{1,2}, Dounia El Yachoui¹, Gerrit S. Gooris¹, Charlotte M. Beddoes¹, Robert M. Dalgliesh³, Marc Malfois⁴, Robert Rissmann^{1,2,5}, and Joke A. Bouwstra^{1,*}

¹Division of BioTherapeutics, Leiden Academic Centre for Drug Research, Leiden University, Leiden, The Netherlands; ²Centre for Human Drug Research, Leiden, The Netherlands; ³ISIS Neutron and Muon Source, Science and Technology Facilities Council, Rutherford Appleton Laboratory, Didcot, United Kingdom; ⁴ALBA Synchrotron, Barcelona, Spain; ⁵Leiden University Medical Center, Leiden, The Netherlands

Abstract The lipids in the uppermost layer of the skin, the stratum corneum (SC), play an important role in the skin barrier function. The three main subclasses in the SC lipid matrix are ceramides (CER), cholesterol, and free fatty acids. In inflammatory skin diseases, such as atopic dermatitis and psoriasis, the SC lipid composition is modulated compared to the composition in healthy SC. One of the main alterations is the molar ratio between the concentration of CER *N*-(tetracosanoyl)-sphingosine (CER NS) and CER *N*-(tetracosanoyl)-phytosphingosine (CER NP), which correlated with an impaired skin barrier function. In the present study, we investigated the impact of varying the CER NS:CER NP ratios on the lipid organization, lipid arrangement, and barrier functionality in SC lipid model systems. The results indicate that a higher CER NS:CER NP ratio as observed in diseased skin did not alter the lipid organization or lipid arrangement in the long periodicity phase encountered in SC. The trans-epidermal water loss, an indication of the barrier functionality, was significantly higher for the CER NS:CER NP 2:1 model (mimicking the ratio in inflammatory skin diseases) compared to the CER NS:CER NP 1:2 ratio (in healthy skin).[■] These findings provide a more detailed insight into the lipid organization in both healthy and diseased skin and suggest that *in vivo* the molar ratio between CER NS:CER NP contributes to barrier impairment as well but might not be the main factor.

Supplementary key words skin • lipids • ceramides • sphingolipids • cholesterol • stratum corneum • fatty acids • lipid organization • barrier function • inflammatory skin diseases

Skin, the largest organ of the human body, has the important role of protecting the body against pathogens, chemicals and radiation, while also preventing excessive water loss (1–3). The outermost layer of the



skin's epidermis is the stratum corneum (SC), with a thickness varying between 10 and 20 μm . It consists of 10–25 layers of corneocytes, which are dead differentiated keratinocytes, embedded in a lipid matrix, and forming a well-organized “brick-mortar” structure (4). The intercellular SC lipid matrix is mainly composed of three lipid classes: ceramides (CER), free fatty acids (FFA), and cholesterol (CHOL) (5, 6). These lipid classes are present at an equimolar ratio (1:1:1) in healthy human SC. Currently, at least 20 CER subclasses have been identified in human SC, which differ based on their head group structure (7–10).

CERs belong to the family of sphingolipids and are formed in the viable epidermis by three general pathways: degradation of glucosylceramides, hydrolysis of sphingomyelin, or de novo synthesis in the endoplasmic reticulum (11). Sphingolipids, together with phospholipids (which are the precursors of FFAs in the epidermis), are structural components of living cell membranes (12). Sphingolipids preferentially associate with CHOL and form lipid rafts, dynamic lateral membrane inhomogeneities, which can interact with membrane proteins and modulate their activity (13). Unlike other biological membranes, the SC lipid matrix does not include phospholipids but contains CHOL (14). Due to the altered lipid composition, the phase behavior in SC is different from the membranes of

*For correspondence: Joke A. Bouwstra, bouwstra@lacdr.leidenuniv.nl.

living cells. However, similar to living cell membranes, CHOL plays an important role in the lipid organization in SC (15, 16).

The intercellular SC lipids are organized as two lamellar phases: a long periodicity phase (LPP), with a repeat distance of 13 nm and a short periodicity phase (SPP), with a repeat distance of 6 nm (17, 18). The LPP is observed exclusively in SC and is assumed to be critical for the skin barrier function (19–22). It was previously shown that for the formation of the LPP, among the various CER subclasses, the esterified ω -hydroxy sphingosine ceramide (CER EOS) and CHOL are crucial (15, 22). In the absence of CER EOS only the SPP is formed (23), while in the absence of CHOL the LPP and SPP are not formed (15). The organization of the lipid chains within this lamellar structure of the SC is referred to as the lateral organization. Based on the density of the packing, this can be orthorhombic (very dense and ordered), hexagonal (less dense, but still ordered), or liquid phase (highly disordered) (24–26). Barrier lipids in human SC are mainly organized in the orthorhombic packing, while a small part of the lipids are packed hexagonally and even small liquid domains are present (27). This is different from phospholipid membranes with high CHOL levels, where a liquid-ordered phase is often encountered (28).

Lipids have been shown to play an important role in the skin barrier function (2, 4). Inflammatory skin diseases, such as atopic dermatitis, seborrheic dermatitis or psoriasis, and the rare hereditary disorder Netherton syndrome, are characterized by a deviation in SC lipid composition, which may contribute to the impaired skin barrier function (J. Rousel *et al.*, unpublished results) (4, 29–31). Clinical studies have revealed that among the lipid compositional alterations of diseased SC, the most prevalent changes are detected in the CER subclass and chain length composition (20, 29, 32–35). A previous study by Yokose *et al.* investigated potential biomarkers in the SC of barrier-disrupted skin and the ratio of CERs in diseased skin (atopic dermatitis and psoriasis) was compared to the CERs ratio in healthy individuals (35). They reported the ratio of CER *N*-(tetracosanoyl)-sphingosine (CER NS) to CER *N*-(tetracosanoyl)-phytosphingosine (CER NP) (Fig. 1) as being a potential marker for impaired skin barrier function in these

patients, as this ratio correlated positively with the trans-epidermal water loss (TEWL). Furthermore, apart from atopic dermatitis and psoriasis, an increased CER NS:CER NP ratio was also reported in the SC of Netherton syndrome patients (34) and recently in seborrheic dermatitis (J. Rousel *et al.*, unpublished results). Therefore, this CER subclass ratio change could be an important factor causing barrier dysfunction in diseased skin. However, the contribution of the altered CER NS:CER NP ratio to the barrier function is not known as in clinical studies the various lipid composition changes always occur simultaneously and only correlations can be obtained.

To understand the relationship between lipid subclasses, lipid models can be used that mimic the organization in the SC lipid matrix. Previous studies showed that lipid models prepared either with isolated pig (36, 37) or human CERs (38), along with CHOL and FFAs mimicked the unique SC lipid organization; the mixtures form the crystalline LPP and SPP, as observed in SC. Furthermore, when isolated porcine or human CER subclasses were replaced by their synthetic counterparts with almost uniform chain length, the phase behavior of the lipid models was similar to the isolated CERs models therefore also closely resembling the lipid organization of native SC (39–42). A further reduction in CER components to 4 or 3 and more recently to only two subclasses showed that when selecting the proper CER subclasses together with CER EOS and mix them with CHOL and FFAs, the models still formed the same lamellar phases and lateral packing (39, 41, 43, 44). This is an important finding as simple models with a limited number of lipid components are compulsory to obtain detailed information about the molecular arrangement, as in these studies a replacement of protiated by deuterated lipids is required.

Lipid models offer the possibility to study changes systematically and to obtain more detailed insights into the underlying factors that cause barrier impairment (45–47). As the CER NS:CER NP ratio was identified as a possible factor for a dysfunctional barrier in inflammatory diseased skin, the aim of the current study is to investigate whether changing the CER NS:CER NP molar ratio results in an altered lipid organization and barrier function in lipid models. A CER composition

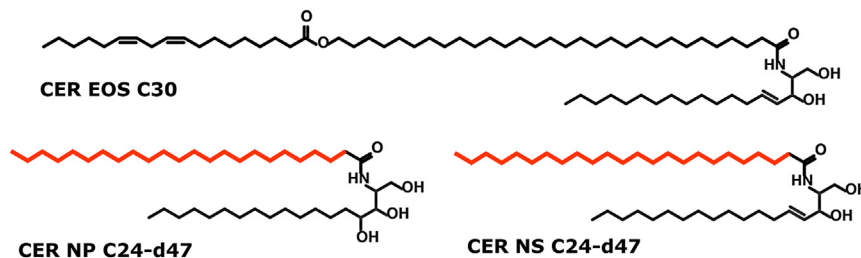


Fig. 1. The molecular structure of the three CERs used in this study. The deuterated acyl chains (d47) of CER NP and CER NS are highlighted in red.

that consists of CER NS, CER NP, and CER EOS, when mixed with CHOL and FFA, has been identified to mimic the phase behavior in SC (48).

In this study, different CER NS:CER NP molar ratios were investigated: 1:2, as observed in healthy SC, 1:1, and 2:1; the latter mimics the approximate ratio observed in inflammatory skin diseases. We decided to use a simple SC lipid model as this allows us to obtain detailed insights about changes in lipid organization and lipid arrangement. In human SC, both the LPP and the SPP are simultaneously present; however, our focus was to examine the influence of the CER NS:CER NP ratio exclusively on the LPP. The lipid organization, lipid arrangement, and barrier functionality were examined in our models. A change in CER NS:CER NP ratio did not induce changes in the lipid organization or the lipid arrangement of CER NS and CER NP in the LPP unit cell. TEWL was increased for the CER NS:CER NP 2:1 model, similarly as observed in clinical studies. These findings imply a contribution of the CER NS:CER NP ratio to the skin barrier impairment in vivo but suggest that this might not be the main factor.

MATERIALS AND METHODS

Materials

Synthetic CER NP and CER NS with acyl chain lengths of 24 carbons (C24) and a sphingosine chain length of 18 carbon atoms (C18), along with CER NP and CER NS with a perdeuterated acyl chain (d47) (NPd47 and NSd47) and CER EOS C30 were kindly donated by Evonik (Essen, Germany). Lignoceric acid (FFA C24) was purchased from Sigma-Aldrich Chemie GmbH (Schnellendorf, Germany) and its deuterated counterpart (DFFA24) was supplied by Arc Laboratories BV (Apeldoorn, The Netherlands). CHOL, deuterium oxide (D₂O), acetate buffer salts, Na₂HPO₄, KH₂PO₄, KCl, and ethyl-p-aminobenzoate (E-PABA) were supplied by Sigma-Aldrich Chemie GmbH (Schnellendorf, Germany). The organic solvents (HPLC grade or higher) were purchased from Biosolve BV (Valkenswaard, The Netherlands). Nucleopore polycarbonate filter disks with a pore size of 0.05 μm (Whatman, Kent, U.K.) were used as sample supports, as well as a silicon substrate obtained from Okmetic (Vantaa, Finland).

Lipid model compositions

An equimolar ratio of CER: CHOL: FFA was selected for the lipid models. The concentration of CER EOS was 40 mol% of the total CERs to allow an exclusive formation of the LPP structure. Furthermore, this also results in a peak separation between crystalline CHOL and the fourth-order diffraction peak of the LPP, irrespective of the CER NS:CER NP ratio. This is crucial for an accurate analysis of the neutron data. The ratio between CER NS:CER NP was changed in the different models (total 60 mol%). Different models were then prepared by substituting CER NS, CER NP or FFA C24 with their deuterated counterparts, as shown in Table 1. For the neutron studies, CER NS and CER NP were substituted with their deuterated counterparts, NSd47 and NPd47 (indicated in the model name). To allow a direct comparison of the results, the same amount of deuterated lipids should be present in the models (20% of total CERs). For this reason, the samples LPP NS:NPd47 1:2 and LPP NSd47:NP 2:1 were prepared with a mix of CER NP:NPd47 (1:1) and CER NS:NSd47 (1:1), respectively. For the FTIR studies, both CER NS and CER NP were entirely substituted in the models with their perdeuterated counterparts, alongside FFA C24 with DFFA.

Preparation of the lipid models

Approximately the same sample preparation method was used for the different analysis techniques and details are provided in Table 2. The necessary amount of lipids was dissolved in the solvent at a concentration of 5 mg/ml. The lipid samples were sprayed using a Camag Linomat IV device (Muttentz, Switzerland) under a gentle stream of nitrogen, at a spraying rate of 14 s/μl. For the samples prepared for permeability and TEWL, a ~12 μm thick lipid layer was obtained (46). All samples were equilibrated using an automatic equilibrators with a heating rate of 4°C/min until reaching 95°C, maintained at this temperature for 65 min to allow the lipid film to melt, and then slowly cooled to 25°C. Prior to the measurements, the samples were hydrated. As different analysis methods required different sample supports and nucleopore polycarbonate disks are not resistant against chloroform/methanol, in that case, we used hexane/ethanol as a solvent. However, this does not affect the formation of the lipid membrane (49).

Permeability

A drug permeation study was performed using Permeagear in-line diffusion cells (Bethlehem, PA, USA) with a diffusion

TABLE 1. Composition of the lipid models used in this study

Model	Lipid Composition	Molar Ratio
LPP NS:NP 1:2	CER EOS C30 : CER NS C24 : CER NP C24 : CHOL : FFAC24	0.4:0.2:0.4:1:1
LPP NS:NP 1:1	CER EOS C30 : CER NS C24 : CER NP C24 : CHOL : FFAC24	0.4:0.3:0.3:1:1
LPP NS:NP 2:1	CER EOS C30 : CER NS C24 : CER NP C24 : CHOL : FFAC24	0.4:0.4:0.2:1:1
LPP NSd47:NP 1:2	CER EOS C30 : CER NS C24-d47 : CER NP C24 : CHOL : FFAC24	0.4: 0.2 :0.4:1:1
LPP NS:NPd47 1:2	CER EOS C30 : CER NS C24 : (CER NP C24 : CER NP C24-d47) : CHOL : FFAC24	0.4:0.2:(0.2: 0.2):1:1
LPP NSd47:NP 2:1	CER EOS C30 : (CER NS C24 : CER NS C24-d47) : CER NP C24 : CHOL : FFAC24	0.4:(0.2: 0.2):0.2:1:1
LPP NS:NPd47 2:1	CER EOS C30 : CER NS C24 : CER NP C24-d47 : CHOL : FFAC24	0.4:0.4: 0.2 :1:1
LPP NSd47:NP:DFFA 1:2	CER EOS C30 : CER NS C24-d47 : CER NP C24 : CHOL : DFFAC24	0.4: 0.2 :0.4:1:1
LPP NS:NPd47:DFFA 1:2	CER EOS C30 : CER NS C24 : CER NP C24-d47 : CHOL : DFFAC24	0.4:0.2: 0.4 :1:1
LPP NSd47:NPd47:DFFA 1:2	CER EOS C30 : CER NS C24-d47 : CER NP C24-d47 : CHOL : DFFAC24	0.4: 0.2 : 0.4 :1:1
LPP NSd47:NP:DFFA 2:1	CER EOS C30 : CER NS C24-d47 : CER NP C24 : CHOL : DFFAC24	0.4: 0.4 :0.2:1:1
LPP NS:NPd47:DFFA 2:1	CER EOS C30 : CER NS C24 : CER NP C24-d47 : CHOL : DFFAC24	0.4:0.4: 0.2 :1:1
LPP NSd47:NPd47:DFFA 2:1	CER EOS C30 : CER NS C24-d47 : CER NP C24-d47 : CHOL : DFFAC24	0.4: 0.4 : 0.2 :1:1

The deuterated lipids are indicated in bold.

TABLE 2. Sample preparation details for each analytical technique used in this study

Technique	Amount of lipids	Solvent	Spraying Area	Sample Support	Hydration
Permeability	1 mg	hexane/ ethanol (2:1, v/v)	1 × 1 cm ²	nucleopore polycarbonate disk	1 h, PBS in diffusion cell, at 32°C
TEWL	1 mg	hexane/ ethanol (2:1, v/v)	1 × 1 cm ²	nucleopore polycarbonate disk	30 min, water in diffusion cell, room temperature
SAXD	1 mg	hexane/ ethanol (2:1, v/v)	2 × 3 mm ²	nucleopore polycarbonate disk	24 h, 80% relative humidity, room temperature
FTIR	1 mg	chloroform/ methanol (2:1, v/v)	1 × 1 cm ²	silver bromide (AgBr) window	≥12 h, acetate buffer (pH 5) in D ₂ O, at 37°C
Neutron diffraction	10 mg	chloroform/ methanol (2:1, v/v)	1.2 × 3.8 cm ²	silicon substrate	≥12 h, D ₂ O/H ₂ O buffer (100%, 50%, 8%), at 37°C

area of 0.28 cm². The acceptor phase was phosphate-buffered saline (PBS, pH 7.4), and the donor phase consisted of a saturated ethyl-p-aminobenzoate (E-PABA) solution (0.65 mg/ml concentration, prepared in acetate buffer with pH 5). The samples were mounted in the diffusion cells and the temperature was maintained at 32°C. The acceptor solution was continuously stirred using a small magnetic stirrer and it had a continuous flow of approximately 2.5 ml/h. To start the experiment, E-PABA was added to the donor compartment, which was then covered with adhesive tape. Every hour fractions of the acceptor phase were collected, over 15 h. At the end of the experiment the PBS flow was determined by weighing the collected tubes and the E-PABA concentration was determined using ultra-high performance liquid chromatography (UPLC), as described below. Each sample group consisted of at least 6 replicates. The steady-state flux of E-PABA was calculated as an average between the 10th and the 15th hours. Statistical analysis was performed using GraphPad Prism 5 using a one-way ANOVA test.

UPLC analysis of E-PABA

UPLC analysis was performed using a validated method, described previously (50). The Acquity UPLC system (Waters) was connected to a UV-VIS detector. The column (1.7 μm siloxane hybrid particles) was maintained at 40°C. The mobile phase consisted of a mixture of 0.1% trifluoroacetic acid in acetonitrile : Milli-Q (40:60 ratio, v/v), with a flow rate of 1 ml/min. Ten μl of each sample and the calibration curve (described previously by Uche *et al.* (50)) were injected.

Trans-epidermal water loss

TEWL was measured using an AquaFlux AF 200 (Biox Systems Ltd.). This method was previously described by Mojumdar *et al.* (51). The AquaFlux device was tightly connected to the donor compartment of the diffusion cell by using a measurement cap (Biox Systems Ltd.). The TEWL flux of the lipid models was recorded for 30 min at a collection rate of 10 s. The average steady-state TEWL in the last 10 min of the measurement was calculated and statistical analysis was performed using an unpaired *t* test in GraphPad Prism 5 to assess the differences between the two groups ($P < 0.05$). At least 10 lipid membranes were measured for each of the two compositions.

X-ray measurements

Small-angle X-ray diffraction (SAXD) measurements were performed at the ALBA Synchrotron (Barcelona, Spain) at the NCD-SWEET beamline. The distance between the detector

(Pilatus 1M detector with a pixel array of 981 × 1043, each pixel: 172 × 172 μm²) and the sample was 2.148 m. The wavelength of the beam was 0.999 Å. The lipid samples were measured at 23°C for 20 s and the setup was calibrated with silver behenate prior to the measurements. Each composition was measured twice.

The two-dimensional scattering plot was integrated over a 90° segment from the beam center to obtain the one-dimensional X-ray intensity profiles of the scattering intensity (*I*) as a function of the scattering vector (*q*). The latter can be calculated as $q = (4\pi \sin \theta) / \lambda$, where θ represents the scattering angle and λ is the wavelength. The peaks were fitted using the Pearson VII function in Fityk (52) to determine the peak positions (q_n). The repeat distance (*d*) of the lamellar phase was calculated by least square fitting using the equation $d = 2n\pi / q_n$, where *n* is the order number of the diffraction peak attributed to a lamellar phase.

FTIR measurements

A Varian 670-IR spectrometer (Agilent Technologies, Santa Clara, USA) fitted with a broadband mercury cadmium telluride detector, cooled by liquid nitrogen, was used to perform the FTIR measurements. The spectra were collected at a resolution of 1 cm⁻¹, by co-addition of 256 scans over 4 min. The sample chamber was continuously purged with dry air for at least 30 min prior to the measurements. The lipid models were measured between 10–90°C, with a heating rate of 0.25°C/min and the wavenumber range of the measurements was 600–4000 cm⁻¹. Data collection and analysis were performed using Resolution Pro software (Agilent Technologies), and the spectra were deconvoluted using a peak half-width of 4 cm⁻¹ and an enhancement factor of 1.4. Three measurements were performed for each composition.

The thermotropic behavior and conformational ordering of the samples were followed by examining the peak positions of the CH₂ and CD₂ symmetric stretching vibrations (ν_s CH₂: wavenumber range 2845–2855 cm⁻¹ and ν_s CD₂: wavenumber range 2080–2100 cm⁻¹). The mid-phase transition temperatures (orthorhombic – hexagonal: T_m O-H; hexagonal – liquid: T_m H-L) were determined by linear regression fitting, as previously described (53). CH₂ and CD₂ scissoring vibrations (δ CH₂, wavenumber range: 1462–1473 cm⁻¹; δ CD₂, wavenumber range: 1085–1095 cm⁻¹) were examined to determine the lipid chain packing and their accurate peak positions were determined by fitting Lorentzian peaks with an in-house Python script. A peak height ratio (OR/MID) was calculated as an average of the peak heights of the two orthorhombic scissoring peaks divided by the peak height of the central scissoring peak, to quantitatively assess the chain interactions for both δ CH₂ and δ CD₂ vibrations. Statistical analysis was

performed to determine the significance of the results obtained from the peak positions (unpaired *t* test, using GraphPad Prism 5; results were statistically different when $P < 0.05$).

Neutron diffraction measurements and data analysis

The lipid arrangement of the two models with CER NS:CER NP ratios of 1:2 and 2:1 was measured using the small-angle neutron scattering (SANS) mode of the LARMOR instrument, at the ISIS Neutron and Muon Source (Rutherford Appleton Laboratory, UK). The samples were measured with a neutron beam size of 1×30 mm, in the wavelength range (λ) between 1 – 12.5 Å and a sample angle to the beam of 2.5° . The ^3He detector was positioned at a distance of 4.4 m from the sample and was set at a 2θ angle of 5° to the direct beam, covering an area of 664×600 mm with a pixel size of 4×8 mm.

The environment of the sample was kept constant using a sealed, heated aluminum chamber, and the windows of the chambers were maintained at 42°C to prevent condensation. Each sample was measured for 4 h ($40 \mu\text{A/h}$ accelerator proton charge) at 25°C for each hydration level. The SANS data were normalized to the incident flux shape and detector efficiency using a direct beam measurement. An empty chamber was used as background measurement, which was subsequently subtracted from each sample.

The Mantid software framework (54) was used to reduce the neutron scattering data to monitor the normalized intensity versus scattering vector (q), resulting in a range of q between 0.032 and 0.991 nm^{-1} . The scattering angle (2θ) was converted to q using Bragg's equation as follows:

$$q = 4\pi \sin \theta / \lambda \quad (1)$$

The repeat distance (d) of the lamellar phase (LPP) was calculated based on the positions of the equidistant Bragg peaks using the following equation:

$$d = 2\pi n / q_n \quad (2)$$

where n is the diffraction order number of the peak at position q_n .

The scattering length density (SLD) profiles were calculated for each sample using the intensity versus q data. The data analysis method has been previously described (55–57). In short, the Bragg peaks were fitted in the Fityk software (using a Pearson VII function) to obtain the intensity value of each diffraction order (52). The structure factor amplitude ($|F_n|$) for each diffraction order was calculated using the following formula:

$$|F_n| = A_n \sqrt{L I_n} \quad (3)$$

The Lorentz correction (L) can be assumed to be $L = q$ because of the high degree of orientation of the lipid lamellae. The correction factor for sample absorption (A_n) can be calculated as:

$$A_n = \frac{1}{\sqrt{\frac{\sin \theta}{2\mu l} \left(1 - e^{-\frac{2\mu l}{\sin \theta}}\right)}} \quad (4)$$

where l represents the lipid sample thickness and μ is the linear attenuation coefficient (58).

The phase signs of $|F_n|$ for the different diffraction orders were calculated using the different $\text{D}_2\text{O}/\text{H}_2\text{O}$ hydration buffer levels (100%, 50%, and 8%), as previously described (48). First, the F_n values were plotted as a function of the D_2O amount in the hydration buffer (supplemental Fig. S1). The LPP unit cell is centrosymmetric, as demonstrated by the linear correlation of the relative structure factor amplitudes as a function of the $\text{D}_2\text{O}/\text{H}_2\text{O}$ buffer shown in supplemental Fig. S1. The water molecules are located close to the hydrophilic lipid head groups, which are positioned at the boundary of the unit cell of the lamellar phases (56, 59, 60). As the structure is symmetric, the water profile phase signs can be either negative or positive. Assuming that the water is located close to the head groups at the boundary of the unit cell, the slopes of the linear correlation of the structure factors and the buffer ratio between 100% and 8% $\text{D}_2\text{O}/\text{H}_2\text{O}$ indicate that the phase signs of the water profile is $-, +, -, +, -, +$ for both CER NS:CER NP 1:2 and 2:1 models. These phase signs are in accordance with previously described LPP phase signs for the water profile (48, 55, 56, 61, 62).

Next, the phase signs of the protiated and deuterated lipid samples were individually determined based on the negative or positive sign of the F_n at 8% $\text{D}_2\text{O}/\text{H}_2\text{O}$ hydration (supplemental Fig. S1) and appeared to be $-, +, -, +, -, +$ for all compositions, including those with partly deuterated lipids.

Using the phase signs and the values for the structure factors, the scattering length density (SLD, $\rho(x)$) profile of the LPP unit cell was plotted using Fourier reconstructions with Equation 5, where x represents the distance in the unit cell (center of the unit cell is $x = 0$) (55):

$$\rho(x) = F_0 + 2 \sum_{n=1}^{n_{\max}} F_n \cos\left(\frac{2\pi nx}{d}\right) \quad (5)$$

The scattering density per unit volume (F_0) was calculated using the chemical composition and density of the lipid sample (63) <https://www.ncnr.nist.gov/resources/activation/>. It included one water molecule per lipid in agreement with the obtained sample hydration (48). The SLD profiles that provide the position of the deuterated lipid chains were obtained from the difference in the SLD profiles of the deuterated and protiated samples, with the two samples hydrated at 8% $\text{D}_2\text{O}/\text{H}_2\text{O}$. This hydration level was chosen as the scattering contribution of the buffer at 8% D_2O is zero; therefore, the SLD profiles displayed only the scattering of the lipids.

The SLD data were calculated on a “relative absolute” scale, following the steps previously described (48, 55, 64, 65). This seemingly contradictory term was adopted to allow the detailed examination and scaling of diffraction data as described by Wiener *et al.* (65). Our set of measurements did not include a sample with terminally deuterated sphingosine chain of CER NS (NSd7) that was used in previous measurements to calculate the relative absolute scale. To correct for this, a scaling factor (S_f) was introduced, which was based on previous measurements using the same settings, analysis procedure and a similar lipid model: LPP CER NS:CER NP 1:1 model (48). S_f is calculated as a ratio of the peak area of NSd7 and NPd47 chains from the CER NS:NP 1:1 model.

Next, the peak area of the NPd47 SLD profile (in the LPP NS:NPd47 2:1 model of this study) was fitted using Fityk. This peak area was then multiplied with S_f to obtain the corrected NPd47 peak area scaled to the previous measurements (SLD_{area}).

The scattering of the 47 deuterium atoms in the NPd47 acyl chain (SLD_{dif}) was calculated by subtracting the

scattering of a protiated CER acyl chain (C23H47) from the scattering of a deuterated CER acyl chain (C23D47).

The factor for calculating the absolute SLD values ($SLD_{correct}$) represents the ratio between the scattering of the 47 deuterium atoms in the NPd47 chain and the corrected peak area of the NPd47 profile:

$$SLD_{correct} = \frac{SLD_{dif}}{SLD_{area}} \quad (6)$$

This $SLD_{correct}$ factor finally was applied to the F_n values, transforming the data to the “relative absolute” scale.

This method resulted in deuterated water peaks at the border of the LPP unit cell having the same density in all samples hydrated at 100% D₂O, including the samples measured with deuterated NSd7 in our previous experiments, as expected.

RESULTS

Increasing the CER NS:CER NP ratio results in a higher TEWL but no effect on E-PABA flux

E-PABA diffusion studies were performed to investigate the effect of increasing the CER NS:CER NP ratio on the permeability of the models (Fig. 2A, B). Figure 2A shows the average E-PABA flux through the lipid model membranes of the three different CER NS:CER NP ratios (1:2, 1:1 and 2:1). The steady state was reached after 10 h and the averaged E-PABA steady-state flux calculated between 10 and 15 h is provided in Fig. 2B. In the three groups ($n \geq 6$), the E-PABA flux was very similar (LPP NS:NP 1:2: $2.0 \pm 0.3 \mu\text{g}/\text{cm}^2/\text{h}$; LPP NS:NP 1:1: $2.0 \pm 0.2 \mu\text{g}/\text{cm}^2/\text{h}$; LPP NS:NP 2:1: $2.2 \pm 0.37 \mu\text{g}/\text{cm}^2/\text{h}$), and thus no significant difference was observed between the models.

TEWL measurements were performed on the two models with the molar ratios LPP NS:NP 1:2 and LPP NS:NP 2:1 (Fig. 2C). The water loss of the LPP NS:NP 2:1 model was significantly higher than for the LPP NS:NP 1:2 model ($2.34 \pm 0.46 \text{ g}/\text{m}^2/\text{h}$ compared to $1.61 \pm 0.48 \text{ g}/\text{m}^2/\text{h}$, $n \geq 10$); $P < 0.01$.

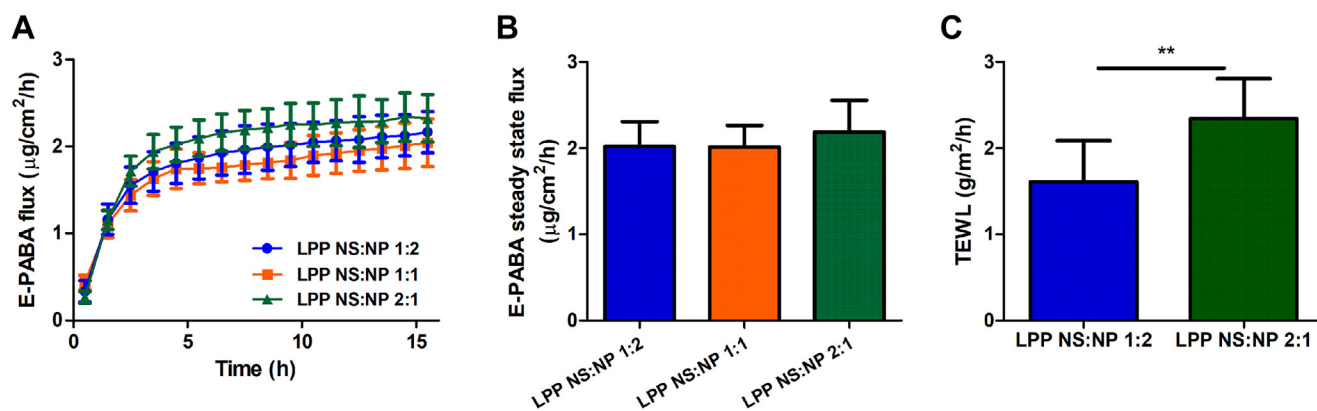


Fig. 2. Permeability of the lipid models. A: The E-PABA flux through the lipid models over 15 h. B: The average steady-state E-PABA flux between 10–15 h ($n \geq 6$). C: TEWL flux across the model membranes, $n \geq 10$ (** $P < 0.01$). All data are presented as mean \pm SD.

CER NS:CER NP ratio does not influence the lamellar or the lateral organization

SAXD studies were performed to obtain information about the lamellar organization of the lipid models and the repeat distances of the lamellar phases of the models with a changed CER NS:CER NP ratio (1:2, 1:1 and 2:1). The diffraction profiles, displayed in Fig. 3A, show a series of nine equidistant peaks, indicating a lamellar phase. The only peaks that could not be assigned to this lamellar structure correspond to the phase-separated crystalline CHOL (with two orders of diffraction at $q = 1.8 \text{ nm}^{-1}$ and $q = 3.6 \text{ nm}^{-1}$; indicated by an asterisk in Fig. 3A). The repeat distance of this lamellar phase is 12.6 nm for the LPP NS:NP 2:1 model, 12.7 nm for the LPP NS:NP 1:1 model, and 12.8 nm for the LPP NS:NP 1:2 model (Table 3) suggesting a slight increasing trend. The peak intensity distribution shows the following order for the first three diffraction peaks: second order has a higher intensity than the first- and third-order peaks (Table 3). This intensity distribution is very characteristic for the LPP and demonstrates the formation of the LPP in all three models (61).

In the next step, the packing of the lipids within the lamellae was examined. Figure 3B shows the δCH_2 vibrations for the protiated LPP NS:NP 1:2 and LPP NS:NP 2:1 models, with two peaks at approximately 1462 cm^{-1} and 1473 cm^{-1} and a small central peak at 1467 cm^{-1} . The exact δCH_2 peak position was determined for each sample by peak fitting using Python scripts, then the δCH_2 peak splitting (distance between the two orthorhombic peaks) and the peak height ratio of the two orthorhombic peaks and the hexagonal central peak (OR/MID) were calculated. Both models had the same δCH_2 peak splitting ($10.6 \pm 0.04 \text{ cm}^{-1}$) and OR/MID peak height ratio (3.00 ± 0.3), therefore no difference in the lateral organization was observed.

Next, the symmetric stretching vibrations were examined as a function of temperature: the thermotropic curves of the $\nu_s\text{CH}_2$ stretching vibrations for the two models are provided in Fig. 3C. At low

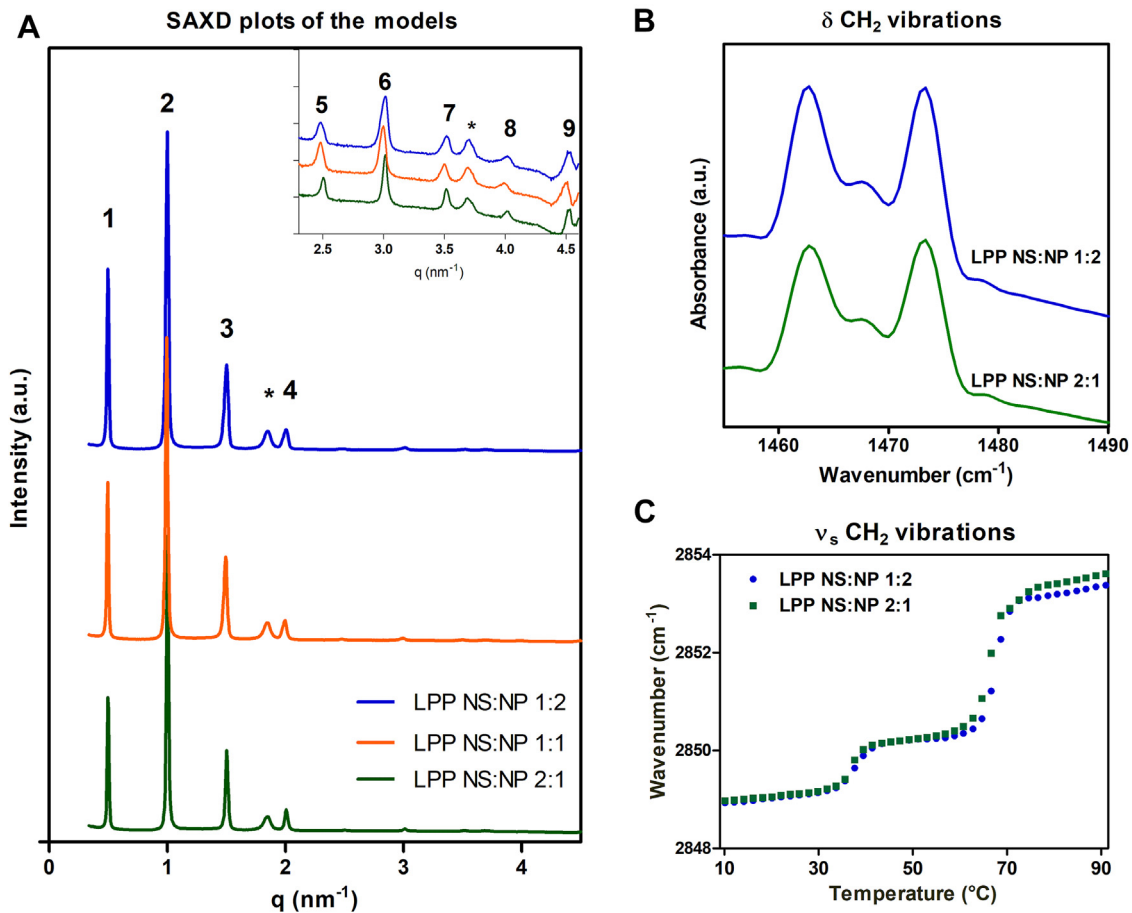


Fig. 3. A: X-ray diffraction profiles of the lipid models. The three CER NS:CER NP ratios: 1:2 (blue), 1:1 (orange) and 2:1 (green). The LPP diffraction orders are indicated with Arabic numbers and the asterisk (*) indicates the phase-separated crystalline CHOL peaks. The insert represents a zoom in of the $q = 2.4\text{--}4.6\text{ nm}^{-1}$ range. B: The δCH_2 vibrations of the two protiated models, measured at 10°C . C: Thermotropic curve of the $\nu_s\text{CH}_2$ vibrations for the protiated samples, LPP NS:NP 1:2 and LPP NS:NP 2:1. The wavenumbers of the $\nu_s\text{CH}_2$ peak position are plotted as a function of temperature ($10\text{--}90^\circ\text{C}$). The FTIR data is shown as an average of 3 measurements for each composition.

temperatures the wavenumber of the stretching vibrations is $<2849\text{ cm}^{-1}$ indicating a high conformational order. This remains constant until 34°C , then there is an increase of the $\nu_s\text{CH}_2$ wavenumber, indicating a lower conformational ordering of the chains. As the scissoring vibrations indicated the presence of an orthorhombic packing at 10°C , this transition is from an orthorhombic to a hexagonal phase, which is confirmed by the scissoring vibrations (not shown). The two mixtures showed similar mid-phase transition temperatures for LPP NS:NP 1:2 ($T_m\text{ O-H } 37.8 \pm 1.2^\circ\text{C}$, $T_m\text{ H-L } 68.7 \pm 1.6^\circ\text{C}$) and LPP NS:NP 2:1 ($T_m\text{ O-H } 36.4 \pm 0.7^\circ\text{C}$, $T_m\text{ H-L } 65.9 \pm 0.3^\circ\text{C}$) (Fig. 3C). Increasing the

TABLE 3. The LPP repeat distance (d-spacing) of the samples shown as average (in nm).

Lipid Model	LPP d-Spacing (nm)	Peak Height Ratio
LPP NS:NP 1:2	12.8	1: 1.8: 0.5
LPP NS:NP 1:1	12.7	1: 1.9: 0.5
LPP NS:NP 2:1	12.6	1: 2.1: 0.5

The peak height ratio is calculated as the ratio between the heights of the fitted peaks for the first: second: third diffraction orders.

temperature further results in a second phase transition from hexagonal to isotropic phase.

Although 32°C is the skin temperature in vivo (also used for the permeability measurements in this study), the conformational order of the lipid models is provided at 10°C , as 32°C is close to the transition temperature from the orthorhombic – hexagonal phase.

Stretching vibrations do not indicate phase separation in the models

The lipid mixing and homogeneity of the samples were examined by replacing protiated chains with their deuterated counterparts. [supplemental Fig. S2 \(Supplementary Material\)](#) displays the thermotropic behavior of the lipid models with deuterated acyl chains of CER NS and CER NP and deuterated FFA (LPP NS:NPd47:DFFA 1:2, LPP:NSd47:NP:DFFA 1:2, LPP NSd47:NPd47:DFFA 1:2, LPP NS:NPd47:DFFA 2:1, LPP:NSd47:NP:DFFA 2:1 and LPP NSd47:NPd47:DFFA 2:1). This shows that for both CER NS:CER NP ratios with deuterated acyl chain of CER NP and DFFA ([supplemental Fig. S2A, D](#)) and with deuterated acyl chain of CER NS and DFFA ([supplemental Fig. S2B, E](#)) a

similar thermotropic response of the $\nu_s\text{CH}_2$ and $\nu_s\text{CD}_2$ vibrations is detected. As an increase of the $\nu_s\text{CH}_2$ wavenumber is observed at $\sim 34^\circ\text{C}$, similar to LPP NS:NP 1:2 and LPP NS:NP 2:1, indicating a shift in the conformational ordering probably caused by an orthorhombic to hexagonal phase transition, as an orthorhombic lateral packing is present at 10°C . The samples with both the acyl chains of CER NS and CER NP and FFAC24 deuterated had a $\nu_s\text{CH}_2$ peak position at $\sim 2850.9\text{ cm}^{-1}$ at 10°C , which was $\sim 0.6\text{ cm}^{-1}$ higher than the samples with only one of the acyl chains deuterated (supplemental Fig. S2C, F). This elevated value represents an indication of a slightly higher conformational disordering of the protiated chains in these two fully deuterated models compared to the chains in the fully protiated samples.

The protiated and deuterated lipids had the same melting behavior in all six models presented in supplemental Fig. S2, with a shift in $\nu_s\text{CH}_2$ and $\nu_s\text{CD}_2$ vibrations starting at $\sim 60^\circ\text{C}$, indicating that the transition from hexagonal to liquid isotropic phase is occurring at approximately the same temperatures (supplemental Table S1). This indicates that the protiated and deuterated lipids undergo phase transitions simultaneously with increasing temperature, implying that the lipid chains mix thoroughly and there are no separated lipid domains in any of the six deuterated models. These results suggest that the altered CER NS:CER NP molar ratio, which only changes the lipid head group structure, does not influence the homogeneous mixing behavior of the compositions with CER NS:CER NP ratio of 1:2 and 2:1. The scissoring vibrations are used to obtain a more detailed insight in the mixing behavior of the lipids, as described below.

Molecular arrangement of the LPP unit is not influenced by the CER NS:CER NP ratio change

The effect of a change in CER NS:CER NP ratio on the location of the deuterated acyl chains of CER NS and CER NP in the LPP unit was examined with SANS. This was studied in models with the CER NS:CER NP ratio of 1:2 and 2:1. The 1D plots of the intensity as a function of the scattering vector q showed equidistant peaks attributed to the LPP (Fig. 4). The d-spacing of the unit cell was calculated and its value was $12.5 \pm 0.03\text{ nm}$ for all samples, without a difference based on the CER NS:CER NP ratio. The phase-separated crystalline CHOL peak was observed at $q = 1.8\text{ nm}^{-1}$ and did not overlap the LPP diffraction peaks, allowing the integration of all the diffraction orders.

The SLD profiles of each model, with the three hydration levels (8%, 50%, and 100% $\text{D}_2\text{O}/\text{H}_2\text{O}$), were determined after the calculation of the structure factors and phase signs (Eq. 5). The water SLD profiles were calculated as the difference between the SLD profile intensity of the protiated sample hydrated at 100% $\text{D}_2\text{O}/\text{H}_2\text{O}$ and the SLD profile intensity of the same sample hydrated at 8% $\text{D}_2\text{O}/\text{H}_2\text{O}$ buffer (Fig. 5A, C). Apart from the two regions at the unit cell border (located at $6.3 \pm 0.1\text{ nm}$ from the center of the unit cell), the water profiles of the two protiated samples (LPP NS:NP 1:2 and LPP NS:NP 2:1) also show two inner water regions positioned at $2.2 \pm 0.1\text{ nm}$ from the center of the unit cell (Fig. 5B, D). The location of the water molecules corresponds to the lipid head group region. This demonstrates that the LPP has a centrosymmetric trilayer structure, in agreement with previous studies (55, 56).

The SLD profiles of the deuterated samples were examined to determine if a change in the CER NS:CER

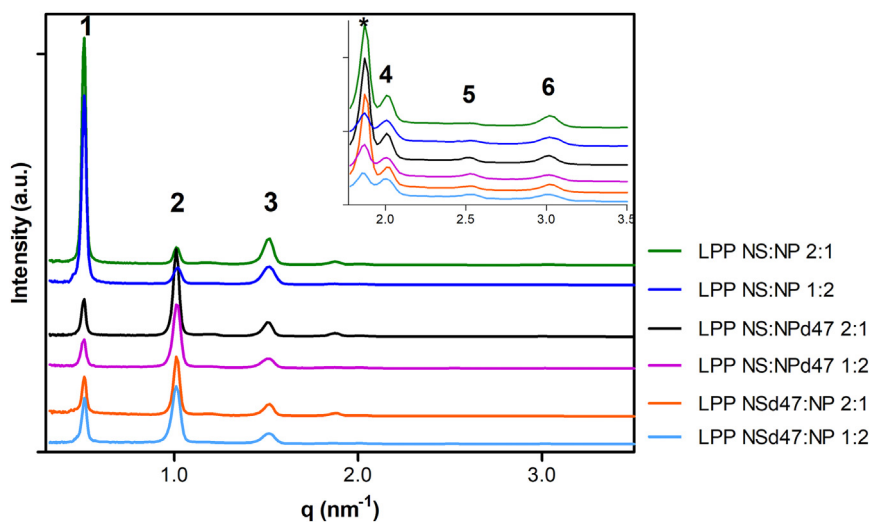


Fig. 4. SANS one-dimensional plots of the six lipid models corresponding to the two CER NS:CER NP ratio systems (1:2 and 2:1), hydrated at 100% $\text{D}_2\text{O}/\text{H}_2\text{O}$ buffer. The intensity plotted as a function of the scattering vector (q) shows the equidistant Bragg peaks corresponding to the first six diffraction peaks of the LPP and the insert displays a zoom-in of the $1.7\text{--}3.5\text{ nm}^{-1}$ region. The phase-separated crystalline CHOL peak is indicated by an asterisk.

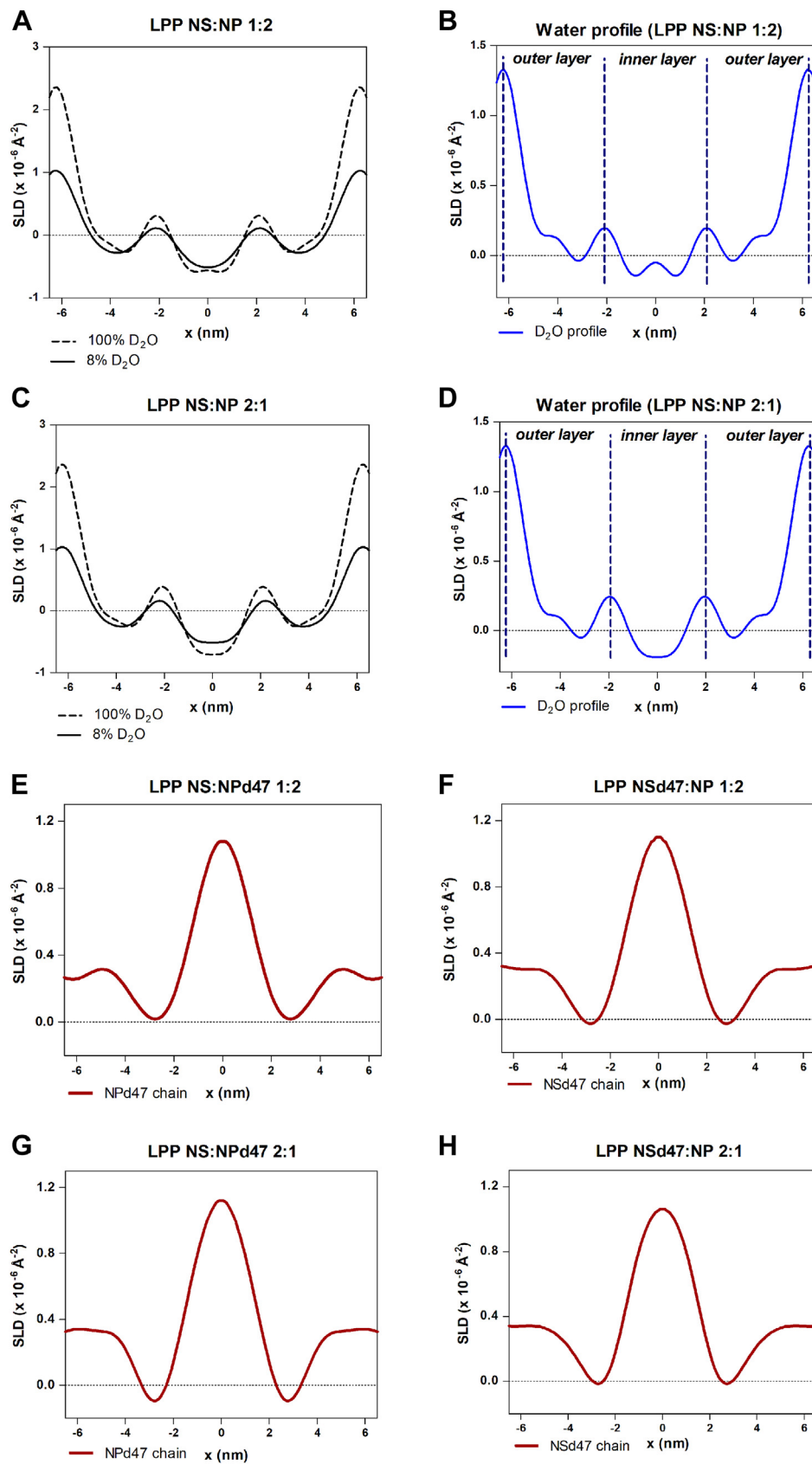


Fig. 5. The neutron SLD profiles of (A) the LPP NS:NP 1:2 protiated sample, measured at 100% D₂O/H₂O hydration and 8% D₂O/H₂O hydration; (B) the resulting water profile of the LPP NS:NP 1:2 sample; (C) LPP NS:NP 2:1 protiated sample, with the two hydration levels 100% D₂O/H₂O and 8% D₂O/H₂O; (D) Water profile of the LPP NS:NP 2:1 model; (E–H) SLD profiles of the acyl chains of CER NP and CER NS in the LPP NS:NP 1:2 models (E, F) and LPP NS:NP 2:1 models (G, H).

NP ratio affected the lipid arrangement in the LPP unit. The positions of the deuterated acyl chains of CER NS and CER NP were determined by subtracting the SLD profile of the protiated sample from the SLD profile of the deuterated sample, both hydrated at 8% D₂O/H₂O buffer. The 8% D₂O/H₂O hydrated models were used, as there is no contribution of water to the SLD profile at this ratio. The resulting SLD profiles indicated the positions of the deuterated moieties in the LPP unit (Fig. 5E–H). The SLD profile corresponding to the LPP NS:NPd47 1:2 model displayed a high SLD intensity in the center of the unit cell; however, a slight elevation of the SLD was also observed in the outer layers of the LPP (Fig. 5E). This suggests that the deuterated acyl chain of CER NP is predominantly located in the central layer of the LPP, with a small fraction located in the outer layers at the unit cell boundary. The SLD profile of the LPP NSd47:NP 1:2 model showed the same distribution, indicating that the acyl chain of CER NS has the same location as the acyl chain of CER NP (Fig. 5F).

Increasing the CER NS concentration (LPP NS:NP 2:1 model) did not influence the location of the acyl chains of CER NS and CER NP in the LPP unit of this model, as the same arrangement of the lipids was observed (Fig. 5G, H). Each lipid model consisted overall of 20% NSd47 or NPd47, which represents 6.6% of total lipids, to ensure an equal number of deuterated chains to be examined by neutron diffraction and to avoid an overload of the detector. The relative absolute intensities of the SLD profiles were similar among the models indicating that the change of the CER NS:CER NP ratio did not result in any differences between the positions of the deuterated acyl chains of CER NS and CER NP in the LPP unit.

CER NS and CER NP both adopt the extended conformation regardless of the CER NS:CER NP ratio

The interaction of the lipid chains was further investigated by examining the shape and the splitting of the δCD_2 (Fig. 6A, B) and δCH_2 vibrations in the FTIR spectra (Fig. 6C, D). When hydrocarbon chains are packed close to each other (orthorhombic packing), the CH₂ groups interact and CH₂-CH₂ short-range coupling occurs creating two peaks in the δCH_2 vibrations. The δCH_2 peak splitting distance depends on the size of the formed orthorhombic lipid domain. A splitting of the scissoring vibrations is also noticed for deuterated samples where the CH₂ chains are replaced by CD₂ chains. The δCH_2 and δCD_2 vibrations have a large vibrational energy difference (CH₂ in the range of 1470 cm⁻¹ and for CD₂ around 1090 cm⁻¹). In deuterated lipid models, if the deuterated chains are located in close proximity forming large domains, the δCD_2 peak to peak distance increases. It reaches a maximum peak-to-peak distance when the domains are around

100 chains (66, 67). The δCD_2 peak positions are around 1085 cm⁻¹ and 1091 cm⁻¹, inducing a very deep minimum. However, when protiated and deuterated chains are neighboring and participate in the same orthorhombic lattice, CH₂-CD₂ chain interactions occur and as a consequence of the different vibrational energy, the short-range coupling of the CD₂-CD₂ chains is lost. This results in the formation of a central single peak in the δCD_2 vibration at around 1088.5 cm⁻¹, located between 1085 cm⁻¹ and 1091 cm⁻¹, thus a shallower depth between the two orthorhombic peaks is observed.

A smaller δCD_2 splitting distance indicates a decreased deuterated lipid domain size. For pure DFFA24 the peak splitting value is 7.3 ± 0.1 cm⁻¹, which is the maximum splitting that can be obtained for large deuterated domains (not shown). In the lipid model LPP NSd47:NPd47:DFFA 1:2, where the acyl chains of both CER NS and CER NP are deuterated together with DFFA, the calculated δCD_2 peak splitting distance is 6.2 ± 0.1 cm⁻¹ (Table 4). This demonstrates that large deuterated lipid domains are formed in the system. To be able to form such large domains, a majority of DFFA chains should be located in proximity of the deuterated acyl chains of CER NS and CER NP in the central layer of the LPP unit. To examine whether domains of mixed protiated and deuterated lipids occur, resulting in CD₂-CH₂ interaction, the peak height ratio between the two orthorhombic scissoring modes (OR: 1085 cm⁻¹ and 1091 cm⁻¹) and the central scissoring mode (MID: 1088.5 cm⁻¹) was calculated by peak fitting, resulting in a value of 5.5 ± 0.1 (OR/MID ratio; Table 4). This value indicates a low number of CD₂-CH₂ interactions compared to the CD₂-CD₂ interactions. As sphingosine and phytosphingosine chains are protiated, this demonstrates that the sphingosine chains are hardly present in the central layer of the LPP.

When CER NPd47 is replaced by protiated CER NP resulting in the LPP NSd47:NP:DFFA 1:2 model, the δCD_2 peak splitting reduces to 4.8 ± 0.1 cm⁻¹, indicating smaller deuterated lipid domains (Table 4). The OR/MID peak height ratio of this sample is decreased in comparison with the model with three deuterated lipids described above, resulting in a value of 3.8 ± 0.1 , indicating that in this sample there are relatively less CD₂-CD₂ chain interactions compared to the CD₂-CD₂ chain interactions in the LPP NSd47:NPd47:DFFA 1:2 model. This demonstrates that the deuterated CER NP acyl chain was a significant part of the deuterated domain formed in the LPP NSd47:NPd47:DFFA 1:2 system.

Next, CER NSd47 was exchanged for the protiated CER NS (LPP NS:NPd47:DFFA 1:2 model). The δCD_2 peak splitting distance of this model is 5.4 ± 0.1 cm⁻¹, which is also a lower value compared to the LPP NSd47:NPd47:DFFA 1:2 model, indicating that the acyl chain of CER NS was also part of the large deuterated domains. The values of the δCD_2 peak splitting distance and peak height ratio are also lower in comparison with

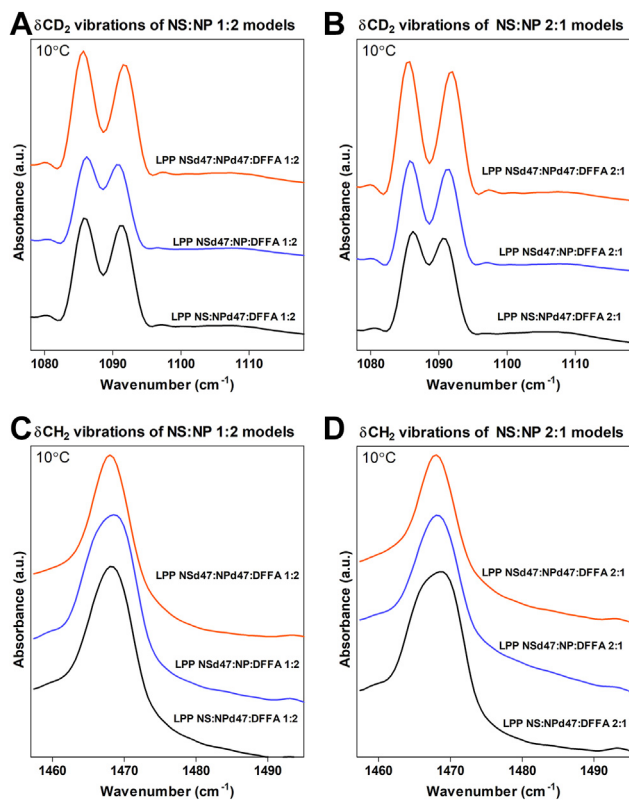


Fig. 6. A: The δCD_2 vibrations for the partially deuterated CER NS:CER NP 1:2 ratio models. B: CER NS:CER NP 2:1 ratio models measured at 10°C. C: The δCH_2 vibrations for the CER NS:CER NP 1:2 models. D: CER NS:CER NP 2:1 models. Each lipid model is annotated in the graph. The δCD_2 peak splitting values were calculated as the difference between the peak positions of the two peaks and are listed in Table 4.

the LPP:NS:NPd47:DFFA 1:2 model, as shown by the data in Table 4. This difference is caused by the lower concentration of CER NS compared to CER NP in the LPP NS:NP 1:2 ratio model (CER NS represents 20% of the total CERs, while the CER NP concentration is 40%).

When analyzing the lipid models with the CER NS:CER NP ratio of 2:1, a similar trend to the 1:2 models was observed (Fig. 6B). The fully deuterated model (LPP NSd47:NPd47:DFFA 2:1) has a large δCD_2 peak splitting distance of $6.3 \pm 0.0 \text{ cm}^{-1}$, comparable to the 1:2 model with the same deuterated lipids composition. This indicates that the size of the deuterated domains in the two compositions is very similar. Furthermore, comparable results are obtained for the partially deuterated models LPP NSd47:NP:DFFA 2:1 and LPP NS:NPd47:DFFA 2:1, where the δCD_2 peak splitting distance is $5.5 \pm 0.1 \text{ cm}^{-1}$ and $4.7 \pm 0.1 \text{ cm}^{-1}$ and the OR/MID peak height ratios of 5 and 3.9 respectively (Table 4). This reveals that the deuterated acyl chains of CER NS and CER NP are indeed part of the large deuterated domains of the CER NS:CER NP 2:1 models. The difference in the δCD_2 peak splitting values between the LPP NSd47:NP:DFFA 2:1 and LPP NS:NPd47:DFFA 2:1 models (observed from Fig. 6B and

Table 4) are caused by the different concentrations of the deuterated CER NS and CER NP in the model.

When comparing the peak splitting of the LPP NSd47:NP:DFFA with the LPP NS:NPd47:DFFA models, the peak splitting distances and δCD_2 peak height ratios were similar when the same fraction of deuterated CERs was compared for both the 1:2 and the 2:1 models (Table 4).

The δCH_2 vibrations of all these partially deuterated LPP models show a single peak at 1468 cm^{-1} at 10°C (Fig. 6C, D). This indicates that the protiated lipid chains were well mixed with the deuterated lipid chains and they did not form phase-separated protiated lipid domains. Possibly a fraction of the protiated chains may also be in a hexagonal packing contributing to the single peak at 1468 cm^{-1} . Figure 6C and D also indicate that the δCH_2 vibrations of the LPP NSd47:NP:DFFA 1:2 and LPP NS:NPd47:DFFA 2:1 models show a broader peak. The lower level of deuterated lipid compared to the models LPP NS:NPd47:DFFA 1:2 and LPP NSd47:NP:DFFA 2:1 may play a role here as this reduced the $\text{CD}_2\text{-CH}_2$ interactions and increased the $\text{CH}_2\text{-CH}_2$ interactions.

DISCUSSION

In living cell membranes, CERs are in competition with CHOL to interact with the amide group of sphingomyelin by forming a network of hydrogen bonds. These interactions are of interest as they play a role in the formation of lipid rafts (68). In SC, the situation is different as hardly no phospholipids are present. However, CHOL and CERs form stable membranes, even in the absence of FFAs, and strongly interact with each other (38). This strong interaction is important, as the SC serves as a barrier to minimize the permeation of compounds to the viable epidermis.

The present study aimed to investigate the effect of changing the CER NS:CER NP molar ratio on the composition of a simple lipid model consisting of CER EOS, CER NS, CER NP, CHOL, and FFA C24. The lipid organization, lipid chain interactions, lipid arrangement, and barrier functionality of these models were examined, as previous studies have shown that an altered CER NS:CER NP ratio represents one of the lipid compositional changes in the SC of inflammatory skin diseases (29, 33–35). The results of this study showed that the position of CER NS and CER NP in the unit cell is very similar and that varying the CER NS:CER NP ratio (1:2 and 2:1) did not influence the location of the acyl chains of CER NS and CER NP in the LPP unit. Both of these acyl chains were mainly positioned in the inner layer, but with a minor part located in the outer layers of the LPP, similar to a recent study on an LPP model with a CER NS:CER NP 1:1 ratio (48). A schematic drawing of the unit cell lipid arrangement is provided in supplemental Fig. S3.

Lipid models prepared either with isolated CERs (porcine or human origin) or synthetic CERs, with CHOL

TABLE 4. δCD_2 peak splitting and the δCD_2 peak height ratio (OR/MID) of the six deuterated LPP models, at 10°C

Lipid Model	δCD_2 Peak Splitting (cm^{-1})	δCD_2 Peak Height Ratio (OR/MID)
LPP NSd47:NP:DFFA 1:2	4.8 ± 0.1	3.8 ± 0.1
LPP NS:NPd47:DFFA 1:2	5.4 ± 0.1	5.0 ± 0.0
LPP NSd47:NPd47:DFFA 1:2	6.2 ± 0.0	5.4 ± 0.1
LPP NSd47:NP:DFFA 2:1	5.5 ± 0.1	5.0 ± 0.0
LPP NS:NPd47:DFFA 2:1	4.7 ± 0.1	3.9 ± 0.1
LPP NSd47:NPd47:DFFA 2:1	6.3 ± 0.0	5.5 ± 0.1

Data are shown as an average of 3 measurements for each composition ± SD.

and FFAs, have been shown to mimic the unique phase behavior of native SC (36–41). Previous studies reported the same lipid organization and molecular arrangement both in lipid models with a larger number of lipid subclasses (complex models) and in simpler compositions with only two CER subclasses (48, 55, 62). This important finding allowed the use of lipid models with a limited number of components for understanding the molecular arrangement of lipids in SC models. Thus, the findings of this study using simple lipid compositions can be extrapolated both to the complex lipid models (with synthetic or isolated CERs) and to the SC lipid matrix.

The similar arrangement and location of CER NS and CER NP in the LPP unit cell regardless of the molar ratios represent an indication of the adaptability of the SC lamellar phase to changes in the lipid head group structure. This can represent a possible reason why the CER composition in murine and porcine SC (both having CER NS as the most abundant CER subclass) is very different from that in human SC (having CER NP as an abundant CER subclass), while the phase behavior in SC of these three species is very similar (10, 69). The linear conformation of the CERs in these lipid models allows a tighter packing of the lipid chains, which is favorable for the skin barrier. Overall, apart from the relevance to inflammatory skin diseases, the results of this study enhance the understanding of the lipid organization in SC of various species.

Location and conformation of CER NS and CER NP not affected by the changes in the composition

Neutron diffraction was used to localize the acyl chains of CER NS and CER NP in the LPP unit of the LPP NS:NP 1:2 and LPP NS:NP 2:1 models. The SLD profiles obtained showed that the deuterated acyl chains of CER NS and CER NP had the same location in the LPP unit cell, predominantly in the central layer, with a small fraction in the outer layers of the repeating unit, for both the CER NS:CER NP 1:2 and 2:1 models. The large splitting of the δCD_2 vibrations in the FTIR spectra revealed large deuterated lipid domains in the LPP of the models LPP NSd47:NPd47:DFFA (1:2 and 2:1 ratio), suggesting that the deuterated acyl chains of CER NS, CER NP, and DFFA are neighboring. Therefore, it can be concluded that the CER acyl chains

and the FFA are in close proximity in the inner layer of the LPP unit cell.

Besides the large splitting, the deep minimum between the two δCD_2 peaks of the LPP NSd47:NPd47:DFFA model also indicates that the $\text{CD}_2\text{-CH}_2$ interactions are reduced to a minimum in the two models. Therefore, CER NS and CER NP with the headgroup located in the two central head group regions adopt primarily an extended conformation, allowing for the acyl chains and FFAs to be in close proximity in the inner layer. It is unlikely that the deuterated acyl chains of CER NS and CER NP interact with the protonated sphingoid bases of these CERs (as would be the case if the CERs adopted hairpin conformations) as this would introduce extensive $\text{CD}_2\text{-CH}_2$ interactions. Furthermore, our results demonstrate that the conformations of CER NS and CER NP are not influenced by the change in the CER NS:CER NP molar ratio. A similar location of the acyl chains of CER NS and CER NP and an extended conformation of these CERs were also encountered in a LPP NS:NP 1:1 model, described in a recent study (48).

The results of this study demonstrate the adaptability of the LPP unit cell organization to changes in the CER head group architecture: partial replacement of CER NS that has a double bond close to the head group region by CER NP with a C4-hydroxyl group on that position does not affect the lipid arrangement in the unit cell of the LPP.

Choice of CER NS:CER NP ratio for the models

In inflammatory skin diseases such as atopic dermatitis, psoriasis, and Netherton syndrome, alongside an altered SC lipid composition and organization compared to control SC, an altered skin barrier function has been reported, often monitored by TEWL (4, 29–31). A strong correlation has been shown between an increased CER NS:CER NP molar ratio and elevated TEWL (35), which might therefore represent an important contribution to the impaired skin barrier function. In healthy SC, the approximate molar ratio of CER NS:CER NP is 1:2.3, while in diseased skin, it is increased to 1:1 or even higher, depending on the severity of the disease (4, 35). Therefore, in this study, we used a CER NS:CER NP 1:2 M ratio as a model for control (healthy) skin, while the models with a CER NS:CER NP ratio 2:1 and CER NS:CER NP 1:1 used in our previous study mimic the variation in ratios observed in diseased skin (48). Similarly, as in patients with atopic eczema, we observed an elevated TEWL when increasing the CER NS:CER NP ratio, an indication that a CER head group change results in an impaired skin barrier function. However, we did not observe an increase in the flux of E-PABA through the lipid membrane. As the hydrogen bonding between the head groups is more extensive for CER NP than for CER NS (70, 71), this may cause the water molecules to interact more with the CER head groups in the LPP NS:NP 1:2

model, forming hydrogen bonds and reducing the TEWL flux. Due to its structure, E-PABA may form fewer hydrogen bonds with the CER headgroup and this could be a reason for the similar E-PABA flux of the two models.

In this study, we varied CER NS:CER NP ratio while keeping the CER chain lengths equal. Previous clinical studies observed that in patients with atopic dermatitis, psoriasis, and seborrheic dermatitis the CER NS:CER NP ratio correlates with the TEWL (J. Rousel *et al.*, unpublished results) (35, 72). However, besides the increase in the CER NS:CER NP ratio, a simultaneous reduction in chain length also occurs in vivo, as the CER NS subclass contains a higher level of CER C34 than CER NP (20, 21, 73). Since we keep the CER chain lengths the same in our models, we demonstrate that a change exclusively in the CER NS:CER NP molar ratio affects the lipid barrier. A recent study by Rousel *et al.* also showed a strong correlation between the CER NS:CER NP total ratio and the TEWL in SC of seborrheic dermatitis patients (J. Rousel *et al.*, unpublished results). In this study, when narrowing the chain length distribution of CER NS and CER NP between C40 and C53 (total number of carbon atoms) while excluding the influence of C34 CERs, an excellent correlation between the molar ratio CER NS:CER NP and TEWL is still observed in patients (supplemental Fig. S4), confirming that the change in CER head group ratio plays a role in the impaired skin barrier function as well. In agreement with our results, another study showed that the permeability of an LPP lipid membrane comprised of 60% CER NS C24 / 40% CER EOS was also significantly higher than that of a model with 60% CER NP / 40% CER EOS (50).

Conformational ordering of the lipid models


An increase in the $\nu_s\text{CH}_2$ wavenumber at 10°C was observed for the LPP NSd47:NPd47:DFFA (1:2 and 2:1 ratios) models in comparison with the protiated samples LPP NS:NP (1:2 and 2:1) and the LPP NSd47:NP:DFFA and LPP NS:NPd47:DFFA models. Possibly the sphingoid bases have a lower conformational ordering than the acyl chain of the CERs and FFAs and a fraction of these might be in a hexagonal packing, as also indicated by the single peak in the δCH_2 vibrations in the membranes of the LPP NSd47:NPd47:DFFA 1:2 and 2:1 ratios, as the level of deuterated chains in the outer layers is expected to be low. However, an increase can also be caused by changes in intermolecular coupling between the chains, which increases the frequency of the $\nu_s\text{CH}_2$ wavenumber in the partly deuterated samples (74). This effect is more pronounced for the $\nu_s\text{CH}_2$ vibration, as intermolecular coupling does not affect the $\nu_s\text{CH}_2$ and $\nu_s\text{CD}_2$ bands to the same extent. The $\nu_s\text{CH}_2$ vibrations of the deuterated models (LPP NSd47:NPd47:DFFA 1:2 and 2:1 ratios) show an increase of the wavenumber between 30-40°C,

characteristic for a phase transition from orthorhombic to hexagonal packing; however, there is a singlet observed in the δCH_2 vibrations. These results indicate that besides the hexagonal packing, a part of the protiated lipids is in an orthorhombic phase: sphingosine chain of CER NS, phytosphingosine chain of CER NP, alongside the CER EOS and CHOL, which are all located in the outer layers of the LPP unit cell (supplemental Fig. S3). The increased width of the singlet peak of the δCH_2 vibrations at 1468 cm^{-1} in the LPP NSd47:NP:DFFA 1:2 and LPP NS:NPd47:DFFA 2:1 compositions indicates that indeed small fractions of the acyl chains of CER NS and CER NP are present in the outer layers of the LPP, partitioning in an orthorhombic packing.

CONCLUSION

This study investigated the effect of systematically changing the molar ratio of CER NS and CER NP in lipid models that mimic the lipid organization of the SC. This is one of the lipid compositional changes previously reported in inflammatory skin diseases correlating with skin barrier impairment. Our findings show that an increased CER NS:CER NP molar ratio (mimicking the diseased SC ratio) does not alter the lipid organization and molecular arrangement of the LPP, while the TEWL was increased in the LPP NS:NP 2:1 model, suggesting an impaired barrier function for water. This indicates that the CER NS:CER NP molar ratio might impair the skin barrier function irrespective of a change in chain length observed simultaneously in clinical studies. The similar lipid organization and arrangement reported in the lipid models investigated in this study demonstrate the adaptability of the LPP to small changes in the CER head group structure.

Data availability

All data are included in the manuscript and supporting information. 

Supplemental data

This article contains [supplemental data \(48\)](#).

Acknowledgments

We thank Prof. Dr. A. Bunge (Colorado School of Mines, U.S.A.) and Prof. Dr. C. McCabe (Heriot-Watt University, U.K.) for the critical reading of the manuscript. We thank the personnel at ISIS Neutron and Muon Source (Didcot, United Kingdom) and ALBA Synchrotron (Cerdanyola del Vallès, Spain) for awarding us experimental beam time and their kind assistance during the measurements. ISIS raw neutron data DOI: [10.5286/ISIS.E.RB1969003](https://doi.org/10.5286/ISIS.E.RB1969003) (75). We are grateful to Evonik (Essen, Germany) for their donation of the CERs. This study was supported by the National Institute of Arthritis and Musculoskeletal and Skin Diseases, grant number R01AR072679.

Author contributions

A. N., J. A. B. Conceptualization; A. N., J. R., D. E. Y., C. M. B. Investigation; A. N. Validation; A. N. Data curation; A. N. Visualization, A. N. Writing – Original draft; J. R., D. E. Y., G. S. G., C. M. B., R. M. D., M. M., R. R., J. A. B. Writing – Review & Editing; G. S. G., M. M. Software; G. S. G., R. M. D., M. M. Resources; R. R., J. A. B. Supervision; J. A. B. Project administration; J. A. B. Funding acquisition.

Author ORCIDiDs

Andreea Nădăban  <https://orcid.org/0000-0002-4981-6268>

Jannik Rousel  <https://orcid.org/0000-0003-0986-3753>

Gerrit S. Gooris  <https://orcid.org/0000-0002-9466-3125>

Robert M. Dalgliesh  <https://orcid.org/0000-0002-6814-679X>

Marc Malfois  <https://orcid.org/0000-0001-5231-1896>

Funding and additional information

This research was supported by the National Institutes of Health grant: National Institute of Arthritis and Musculoskeletal and Skin Diseases [grant number R01AR072679].

Conflict of interest

The authors declare that they have no known competing financial interests or personal relationships that could have appeared to influence the work reported in this paper.

Abbreviations

CER, ceramide; CHOL, cholesterol; DFFA, perdeuterated FFA; E-PABA, ethyl-p-aminobenzoate; FTIR, Fourier-transform infrared spectroscopy; LPP, long periodicity phase; NP, *N*-(tetracosanoyl)-phytosphingosine CER; NPd47, CER NP with a perdeuterated acyl chain (d47); NS, *N*-(tetracosanoyl)-sphingosine CER; NSd47, CER NS with a perdeuterated acyl chain (d47); SANS, small-angle neutron scattering; SAXD, small-angle X-ray diffraction; SC, stratum corneum; SLD, scattering length density; SPP, short periodicity phase; TEWL, trans-epidermal water loss.

Manuscript received March 9, 2023, and in revised form May 15, 2023. Published, JLR Papers in Press, June 8, 2023, <https://doi.org/10.1016/j.jlr.2023.100400>

REFERENCES

1. Proksch, E., Brandner, J. M., and Jensen, J.-M. (2008) The skin: an indispensable barrier. *Exp. Dermatol.* **17**, 1063–1072
2. Madison, K. C. (2003) Barrier function of the skin: "la raison d'être" of the epidermis. *J. Invest. Dermatol.* **121**, 231–241
3. Wertz, P. W., and van den Bergh, B. (1998) The physical, chemical and functional properties of lipids in the skin and other biological barriers. *Chem. Phys. Lipids*. **91**, 85–96
4. van Smeden, J., Janssens, M., Gooris, G. S., and Bouwstra, J. A. (2014) The important role of stratum corneum lipids for the cutaneous barrier function. *Biochim. Biophys. Acta*. **1841**, 295–313
5. Wertz, P. W., Miethke, M. C., Long, S. A., Strauss, J. S., and Downing, D. T. (1985) The composition of the ceramides from human stratum corneum and from comedones. *J. Invest. Dermatol.* **84**, 410–412
6. Weerheim, A., and Ponc, M. (2001) Determination of stratum corneum lipid profile by tape stripping in combination with high-performance thin-layer chromatography. *Arch. Dermatol. Res.* **293**, 191–199
7. t'Kindt, R., Jorge, L., Dumont, E., Couturon, P., David, F., Sandra, P., et al. (2012) Profiling and characterizing skin ceramides using reversed-phase liquid chromatography-quadrupole time-of-flight mass spectrometry. *Anal. Chem.* **84**, 403–411
8. Masukawa, Y., Narita, H., Shimizu, E., Kondo, N., Sugai, Y., Oba, T., et al. (2008) Characterization of overall ceramide species in human stratum corneum. *J. Lipid Res.* **49**, 1466–1476
9. van Smeden, J., Hoppel, L., van der Heijden, R., Hankemeier, T., Vreeken, R. J., and Bouwstra, J. A. (2011) LC/MS analysis of stratum corneum lipids: ceramide profiling and discovery. *J. Lipid Res.* **52**, 1211–1221
10. Kawana, M., Miyamoto, M., Ohno, Y., and Kihara, A. (2020) Comparative profiling and comprehensive quantification of stratum corneum ceramides in humans and mice by LC/MS/MS. *J. Lipid Res.* **61**, 884–895
11. Mizutani, Y., Mitsutake, S., Tsuji, K., Kihara, A., and Igarashi, Y. (2009) Ceramide biosynthesis in keratinocyte and its role in skin function. *Biochimie*. **91**, 784–790
12. Brown, R. E. (1998) Sphingolipid organization in biomembranes: what physical studies of model membranes reveal. *J. Cell Sci.* **111**, 1–9
13. Lingwood, D., and Simons, K. (2010) Lipid rafts as a membrane-organizing principle. *Science*. **327**, 46–50
14. Ponc, M., Weerheim, A., Lankhorst, P., and Wertz, P. (2003) New Acylceramide in Native and Reconstructed Epidermis. *J. Invest. Dermatol.* **120**, 581–588
15. Mojumdar, E. H., Gooris, G. S., and Bouwstra, J. A. (2015) Phase behavior of skin lipid mixtures: the effect of cholesterol on lipid organization. *Soft Matter*. **11**, 4326–4336
16. Sochorova, M., Audrlicka, P., Cervena, M., Kovacic, A., Kopecna, M., Opalka, L., et al. (2019) Permeability and microstructure of cholesterol-depleted skin lipid membranes and human stratum corneum. *J. Colloid Interf. Sci.* **535**, 227–238
17. White, S. H., Mirejovsky, D., and King, G. I. (1988) Structure of lamellar lipid domains and corneocyte envelopes of murine stratum corneum. *X-ray Diffraction Study Biochem.* **27**, 3725–3732
18. Bouwstra, J. A., Gooris, G. S., van der Spek, J. A., and Bras, W. (1991) Structural investigations of human stratum corneum by small-angle X-ray scattering. *J. Invest. Dermatol.* **97**, 1005–1012
19. Schreiner, V., Gooris, G. S., Pfeiffer, S., Lanzendorfer, G., Wenck, H., Diembeck, W., et al. (2000) Barrier characteristics of different human skin types investigated with X-ray diffraction, lipid analysis, and electron microscopy imaging. *J. Invest. Dermatol.* **114**, 654–660
20. Janssens, M., van Smeden, J., Gooris, G. S., Bras, W., Portale, G., Caspers, P. J., et al. (2012) Increase in short-chain ceramides correlates with an altered lipid organization and decreased barrier function in atopic eczema patients. *J. Lipid Res.* **53**, 2755–2766
21. van Smeden, J., Janssens, M., Boiten, W. A., van Drongelen, V., Furio, L., Vreeken, R. J., et al. (2014) Intercellular skin barrier lipid composition and organization in Netherton syndrome patients. *J. Invest. Dermatol.* **134**, 1238–1245
22. Uche, L. E., Gooris, G. S., Bouwstra, J. A., and Beddoes, C. M. (2021) High concentration of the ester-linked omega-hydroxy ceramide increases the permeability in skin lipid model membranes. *Biochim. Biophys. Acta Biomembr.* **1863**, 183487
23. Bouwstra, J. A., Gooris, G. S., Dubbelaar, F. E., Weerheim, A., IJzerman, A. P., and Ponc, M. (1998) Role of ceramide 1 in the molecular organization of the stratum corneum lipids. *J. Lipid Res.* **39**, 186–196
24. Boncheva, M., Damien, F., and Normand, V. (2008) Molecular organization of the lipid matrix in intact Stratum corneum using ATR-FTIR spectroscopy. *Biochim. Biophys. Acta*. **1778**, 1344–1355
25. Damien, F., and Boncheva, M. (2010) The extent of orthorhombic lipid phases in the stratum corneum determines the barrier efficiency of human skin in vivo. *J. Invest. Dermatol.* **130**, 611–614
26. Mendelsohn, R., Rerek, M. E., and Moore, D. J. (2000) Infrared spectroscopy and microscopic imaging of stratum corneum models and skin. *Phys. Chem. Chem. Phys.* **2**, 4651–4657
27. Björklund, S., Nowacka, A., Bouwstra, J. A., Sparr, E., and Topgaard, D. (2013) Characterization of stratum corneum molecular dynamics by natural-abundance ¹³C solid-state NMR. *PLoS One*. **8**, e61889
28. Demel, R. A., and de Kruyff, B. (1976) The function of sterols in membranes. *Biochim. Biophys. Acta*. **457**, 109–132

29. Motta, S., Monti, M., Sesana, S., Caputo, R., Carelli, S., and Ghidoni, R. (1993) Ceramide composition of the psoriatic scale. *Biochim. Biophys. Acta* **1182**, 147–151
30. Janssens, M., van Smeden, J., Gooris, G. S., Bras, W., Portale, G., Caspers, P. J., *et al.* (2011) Lamellar lipid organization and ceramide composition in the stratum corneum of patients with atopic eczema. *J. Invest. Dermatol.* **131**, 2136–2138
31. Sahle, F. F., Gebre-Mariam, T., Dobner, B., Wohlrab, J., and Neubert, R. H. (2015) Skin diseases associated with the depletion of stratum corneum lipids and stratum corneum lipid substitution therapy. *Skin Pharmacol. Physiol.* **28**, 42–55
32. Imokawa, G., Abe, A., Jin, K., Higaki, Y., Kawashima, M., and Hidano, A. (1991) Decreased level of ceramides in stratum corneum of atopic dermatitis: an etiologic factor in atopic dry skin? *J. Invest. Dermatol.* **96**, 523–526
33. Di Nardo, A., Wertz, P. W., Giannetti, A., and Seidenari, S. (1998) Ceramide and cholesterol composition of the skin of patients with atopic dermatitis. *Acta Derm. Venereol.* **78**, 27–30
34. van Smeden, J., Al-Khakany, H., Wang, Y., Visscher, D., Stephens, N., Absalah, S., *et al.* (2020) Skin barrier lipid enzyme activity in Netherton patients is associated with protease activity and ceramide abnormalities. *J. Lipid Res.* **61**, 859–869
35. Yokose, U., Ishikawa, J., Morokuma, Y., Naoe, A., Inoue, Y., Yasuda, Y., *et al.* (2020) The ceramide [NP]/[NS] ratio in the stratum corneum is a potential marker for skin properties and epidermal differentiation. *BMC Dermatol.* **20**, 6
36. Bouwstra, J., Gooris, G., Cheng, K., A, W., Bras, W., and Ponec, M. (1996) Phase behavior of isolated skin lipids. *J. Lipid Res.* **37**, 999–1011
37. McIntosh, T. J., Stewart, M. E., and Downing, D. T. (1996) X-ray diffraction analysis of isolated skin lipids: reconstitution of intercellular lipid domains. *Biochemistry.* **35**, 3649–3653
38. Bouwstra, J. A., Gooris, G. S., Dubbelaar, F. E. R., and Ponec, M. (2001) Phase behavior of lipid mixtures based on human ceramides: coexistence of crystalline and liquid phases. *J. Lipid Res.* **42**, 1759–1770
39. Opalka, L., Kovacik, A., Maixner, J., and Vavrova, K. (2016) Omega-O-acylceramides in skin lipid membranes: effects of concentration, sphingoid base, and model complexity on microstructure and permeability. *Langmuir.* **32**, 12894–12904
40. de Jager, M. W., Gooris, G. S., Ponec, M., and Bouwstra, J. A. (2005) Lipid mixtures prepared with well-defined synthetic ceramides closely mimic the unique stratum corneum lipid phase behavior. *J. Lipid Res.* **46**, 2649–2656
41. Uche, L. E., Gooris, G. S., Bouwstra, J. A., and Beddoes, C. M. (2019) Barrier capability of skin lipid models: effect of ceramides and free fatty acid composition. *Langmuir.* **35**, 15376–15388
42. Opálka, L., Kováčik, A., Pullmannová, P., Maixner, J., and Vávrová, K. (2020) Effects of omega-O-acylceramide structures and concentrations in healthy and diseased skin barrier lipid membrane models. *J. Lipid Res.* **61**, 219–228
43. Janssens, M., Gooris, G. S., and Bouwstra, J. A. (2009) Infrared spectroscopy studies of mixtures prepared with synthetic ceramides varying in head group architecture: coexistence of liquid and crystalline phases. *Biochim. Biophys. Acta.* **1788**, 732–742
44. Beddoes, C. M., Gooris, G. S., and Bouwstra, J. A. (2018) Preferential arrangement of lipids in the long-periodicity phase of a stratum corneum matrix model. *J. Lipid Res.* **59**, 2329–2338
45. Basse, L. H., Groen, D., and Bouwstra, J. A. (2013) Permeability and lipid organization of a novel psoriasis stratum corneum substitute. *Int. J. Pharm.* **457**, 275–282
46. de Jager, M., Groenink, W., Bielsa i Guivernau, R., Andersson, E., Angelova, N., Ponec, M., *et al.* (2006) A novel in vitro percutaneous penetration model: evaluation of barrier properties with p-aminobenzoic acid and two of its derivatives. *Pharm. Res.* **23**, 951–960
47. Groen, D., Gooris, G. S., Ponec, M., and Bouwstra, J. A. (2008) Two new methods for preparing a unique stratum corneum substitute. *Biochim. Biophys. Acta.* **1778**, 2421–2429
48. Nádában, A., Gooris, G. S., Beddoes, C. M., Dalgliesh, R. M., and Bouwstra, J. A. (2022) Phytosphingosine ceramide mainly localizes in the central layer of the unique lamellar phase of skin lipid model systems. *J. Lipid Res.* **63**, 100258
49. de Jager, M., Groenink, W., van der Spek, J., Janmaat, C., Gooris, G., Ponec, M., *et al.* (2006) Preparation and characterization of a stratum corneum substitute for in vitro percutaneous penetration studies. *Biochim. Biophys. Acta.* **1758**, 636–644
50. Uche, L. E., Gooris, G. S., Beddoes, C. M., and Bouwstra, J. A. (2019) New insight into phase behavior and permeability of skin lipid models based on sphingosine and phytosphingosine ceramides. *Biochim. Biophys. Acta Biomembr.* **1861**, 1317–1328
51. Mojumdar, E. H., Kariman, Z., van Kerckhove, L., Gooris, G. S., and Bouwstra, J. A. (2014) The role of ceramide chain length distribution on the barrier properties of the skin lipid membranes. *Biochim. Biophys. Acta.* **1838**, 2473–2483
52. Wojdyr, M. (2010) Fityk: a general-purpose peak fitting program. *J. Appl. Crystallogr.* **43**, 1126–1128
53. Oguri, M., Gooris, G. S., Bito, K., and Bouwstra, J. A. (2014) The effect of the chain length distribution of free fatty acids on the mixing properties of stratum corneum model membranes. *Biochim. Biophys. Acta.* **1838**, 1851–1861
54. Arnold, O., Bilheux, J. C., Borreguero, J. M., Buts, A., Campbell, S. I., Chapon, L., *et al.* (2014) Mantis—data analysis and visualization package for neutron scattering and μ SR experiments. *Nucl. Instr. Met. Phys. Res. Section A: Acc. Spectrometers, Detectors Associated Equipment.* **764**, 156–166
55. Mojumdar, E. H., Gooris, G. S., Barlow, D. J., Lawrence, M. J., Deme, B., and Bouwstra, J. A. (2015) Skin lipids: localization of ceramide and fatty acid in the unit cell of the long periodicity phase. *Biophys. J.* **108**, 2670–2679
56. Mojumdar, E. H., Gooris, G. S., Groen, D., Barlow, D. J., Lawrence, M. J., Deme, B., *et al.* (2016) Stratum corneum lipid matrix: location of acyl ceramide and cholesterol in the unit cell of the long periodicity phase. *Biochim. Biophys. Acta.* **1858**, 1926–1934
57. Beddoes, C. M., Gooris, G. S., Barlow, D. J., Lawrence, M. J., Dalgliesh, R. M., Malfois, M., *et al.* (2022) The importance of ceramide headgroup for lipid localisation in skin lipid models. *Biochim. Biophys. Acta Biomembr.* **1864**, 183886
58. Franks, N. P., and Lieb, W. R. (1979) The structure of lipid bilayers and the effects of general anaesthetics: an X-ray and neutron diffraction study. *J. Mol. Biol.* **133**, 469–500
59. Kiselev, M. A., Ryabova, N. Y., Balagurov, A. M., Dante, S., Hauss, T., Zbytovska, J., *et al.* (2005) New insights into the structure and hydration of a stratum corneum lipid model membrane by neutron diffraction. *Eur. Biophys. J.* **34**, 1030–1040
60. Groen, D., Gooris, G. S., Barlow, D. J., Lawrence, M. J., van Mechelen, J. B., Deme, B., *et al.* (2011) Disposition of ceramide in model lipid membranes determined by neutron diffraction. *Biophys. J.* **100**, 1481–1489
61. Groen, D., Gooris, G. S., and Bouwstra, J. A. (2009) New insights into the stratum corneum lipid organization by X-ray diffraction analysis. *Biophys. J.* **97**, 2242–2249
62. Beddoes, C. M., Gooris, G. S., Foglia, F., Ahmadi, D., Barlow, D. J., Lawrence, M. J., *et al.* (2020) Arrangement of ceramides in the skin: sphingosine chains localize at a single position in stratum corneum lipid matrix models. *Langmuir.* **36**, 10270–10278
63. Harroun, T. A., Katsaras, J., and Wassall, S. R. (2006) Cholesterol hydroxyl group is found to reside in the center of a polyunsaturated lipid membrane. *Biochemistry.* **45**, 1227–1233
64. Mojumdar, E. H., Groen, D., Gooris, G. S., Barlow, D. J., Lawrence, M. J., Deme, B., *et al.* (2013) Localization of cholesterol and fatty acid in a model lipid membrane: a neutron diffraction approach. *Biophys. J.* **105**, 911–918
65. Wiener, M. K., G., and White, S. (1991) Structure of a fluid dioleoylphosphatidylcholine bilayer determined by joint refinement of x-ray and neutron diffraction data I. Scaling of neutron data and the distributions of double bonds and water. *Biophys. J.* **60**, 568–576
66. Moore, D. J., Rerek, M. E., and Mendelsohn, R. (1997) Lipid domains and orthorhombic phases in model stratum corneum: evidence from fourier transform infrared spectroscopy studies. *Biochem. Biophys. Res. Commun.* **231**, 797–801
67. Mendelsohn, R., and Moore, D. J. (1998) Vibrational spectroscopic studies of lipid domains in biomembranes and model systems. *Chem. Phys. Lipids.* **96**, 141–157
68. Garcia-Arribas, A. B., Alonso, A., and Goni, F. M. (2016) Cholesterol interactions with ceramide and sphingomyelin. *Chem. Phys. Lipids.* **199**, 26–34
69. Wertz, P. W., and Downing, D. T. (1983) Ceramides of pig epidermis: structure determination. *J. Lipid Res.* **24**, 759–765
70. Rerek, M. E., Chen, H., Markovic, B., Van Wyck, D., Garidel, P., Mendelsohn, R., *et al.* (2001) Phytosphingosine and sphingosine

- ceramide headgroup hydrogen bonding: structural insights through thermotropic hydrogen/deuterium exchange. *J. Phys. Chem. B* **105**, 9355–9362
71. Guo, S., Moore, T. C., Iacovella, C. R., Strickland, L. A., and McCabe, C. (2013) Simulation study of the structure and phase behavior of ceramide bilayers and the role of lipid head group chemistry. *J. Chem. Theor. Comput.* **9**, 5116–5126
72. Ishikawa, J., Narita, H., Kondo, N., Hotta, M., Takagi, Y., Masukawa, Y., *et al.* (2010) Changes in the ceramide profile of atopic dermatitis patients. *J. Invest. Dermatol.* **130**, 2511–2514
73. Boer, D. E. C., van Smeden, J., Al-Khakany, H., Melnik, E., van Dijk, R., Absalah, S., *et al.* (2020) Skin of atopic dermatitis patients shows disturbed beta-glucocerebrosidase and acid sphingomyelinase activity that relates to changes in stratum corneum lipid composition. *Biochim. Biophys. Acta Mol. Cell Biol. Lipids.* **1865**, 158673
74. Kodati, V. R., El-Jastimi, R., and Lafleur, M. (1994) Contribution of the intermolecular coupling and librational mobility in the methylene stretching modes in the infrared spectra of acyl chains. *J. Phys. Chem.* **98**, 12191–12197
75. Bouwstra, J., Gooris, G., Dalglish, R. M., Beddoes, C. M., and Nadaban, A. (2020) Understanding the effect of Ceramide NP concentration on the skin's long periodicity phase - relevant for atopic eczema studies. *STFC ISIS Neutron Muon Source*. <https://doi.org/10.5286/ISIS.E.RB1969003>